M.C. Morelli, A. Guardone
A Simulation Framework for Rotorcraft Ice Accretion and Shedding
Aerospace Science and Technology, Published online 12/10/2021
doi:10.1016/j.ast.2021.107157

A Three-Dimensional Simulation Framework for Modelling Rotorcraft Ice Accretion and Shedding

Myles Morelli[a,b,*], Alberto Guardone[a]

[a] *Department of Aerospace Science and Technology, Politecnico di Milano, Italy*
[b] *School of Engineering, University of Glasgow, United Kingdom*

Abstract

In this work a novel three-dimensional simulation framework for modelling the safety critical problem of rotorcraft ice formation and shedding is presented. To enable an entirely three-dimensional framework, state-of-the-art numerical modelling techniques are adopted and the inter-dependency between the techniques is discussed. The numerical techniques introduced in this work include models to simulate the rotor flow-field, water droplet trajectories and impingement locations, phase change modelling during the ice accretion, and mesh deformation to account for the moving ice boundary. A set of benchmark test cases are initially used for preliminary validation of the icing framework. This allows for a comparison of the collection efficiency and ice shapes with high-quality experimental measurements. Icing wind tunnel tests conducted on the Spinning Rotor Blade (SRB-II) model rotor are used for an assessment of the numerical predictions specific to rotorcraft. Quantities used for comparisons include the ice thickness and shedding location. Numerical predictions are in good agreement with the measured data at all temperatures. Additionally, the outcome of influential parameters which directly impact rotor ice shapes are assessed. In particular, the model for the temperature profiles within the ice layer, and the centrifugally induced movement of the liquid film.

Keywords: Rotorcraft, Ice Accretion, Ice Shedding

*Corresponding author, email address: mylescarlo.morelli@polimi.it

1. Introduction

In-flight icing encounters can jeopardise the performance and handling qualities of rotorcraft and hence pose a serious threat to flight safety [1, 2, 3]. This threat to flight safety arises when ice rapidly alters aerodynamic lifting surfaces such as rotors which are highly sensitive to geometric modifications during flight. Furthermore, ice accretion occurs primarily on the leading edge of lifting surfaces and subsequently changes the state of the boundary layer which can result in premature flow separation [4]. Natural and artificial in-flight icing trails as well as experimental tests on model rotors can be used to understand rotorcraft icing. Nevertheless, each approach has its own limitations and drawbacks. Resultantly, numerical modelling has received interest as an alternative approach towards understanding the rotorcraft icing phenomena by addressing these weaknesses. However, numerical rotorcraft icing predictions are only as credible as the models are reliable. Thence, it is of interest to limit model assumptions to ensure the highest possible fidelity of model predictions.

Prior to discussing rotorcraft icing simulation techniques, it is first beneficial to understand the simulation structure used for predicting fixed-wing aircraft icing. A conventional fixed-wing icing simulation structure routinely involves a three-stage process which iteratively updates to account for unsteady ice accretion. This simulation process is commonly known as multi-step ice accretion and is shown through the use of a diagram in Fig. 1. The first stage involves the use of a flow solver to determine the aerodynamic flow-field around regions exposed to icing such as the wing, fuselage or even pitot tube. The second stage entails the use of a droplet solver to compute the trajectories of supercooled water droplets in the fluid flow to determine their impingement locations and collection efficiency. The third stage concerns the use of an icing solver to calculate the ice shape based on icing models which are dependent on the surface temperature and collection efficiency as well as other influential parameters. Multi-step ice accretion then introduces a fourth stage to update the iced mesh usually through means of mesh deformation techniques.

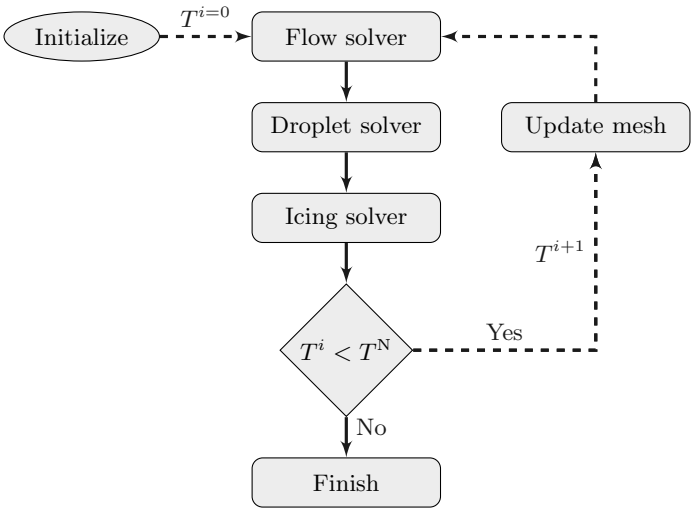

Figure 1: Schematic of a standard multi-step icing simulation.

A brief history of recent techniques developed to simulated rotorcraft icing will now be discussed. A summary of the different numerical modelling techniques introduced in the literature for simulating rotorcraft icing is displayed in Table 1. It highlights the key authors, the period of research development, and the assumptions made when analysing the flow-field, droplet trajectories, and ice accretion.

Between 1991 and 1994, Britton, Bond, and Flemming developed and reviewed the LEWICE icing code for rotorcraft. Together their work played a significant role in the early progress of rotorcraft icing tools [5, 6, 7]. They were part of a Helicopter Icing Consortium which conducted icing experiments on the Power Force Model in the NASA Lewis Icing Research Tunnel [8]. The experimental data was used for code validation with theoretical models. Britton is recognised with the development of an analytical method to predict helicopter main rotor performance in icing conditions [6]. The analytical method was based on the LEWICE code [9] and utilized potential flow theory [10] to describe the flow-field. The local angle-of-attack and velocity at different radial positions was then averaged azimuthally and given as the input to LEWICE due to it be-

ing a steady-state code. The thermodynamic process and freezing fraction was described by Messinger's model [11]. The ice shape computations were therefore two-dimensional in nature at selected radial locations. Flemming is credited with introducing the importance of the role of wind tunnels and computer codes in the certification and qualification of rotorcraft for flight in forecast icing [7]. In 1994 NASA put rotorcraft icing research on hold to focus on fixed-wing icing research due to a number of high profile accidents such as flight 4184 where an American Eagle passenger aircraft crashed causing 64 fatalities [12].

Over a decade later, the numerical modelling of rotorcraft icing garnered new interest and coincided with the development of Computational Fluid Dynamic (CFD) codes which were now able to accurately model three-dimensional flows around rotors. Between 2009 and 2011 a group of established researchers including Sankar, Flemming, Kreeger, Bain, Rajmohan, and Nucci developed a methodology for modelling the effects of ice accretion on rotorcraft performance in hover and forward flight [13, 14, 15, 16]. Their approach was to use a loosely-coupled suite of tools automated in a python framework. A hybrid CFD solver was used to solve the flow-field. The hybrid CFD solver computes the Navier-Stokes equations near a single blade and uses a Lagrangian wake mode in the far-field. The CFD solver was then loosely coupled with a Computational Structural Dynamics (CSD) code to determine the rotor trim. The LEWICE3D code [17] was used at two-dimensional sections along the rotor to compute ice accretion. A three-dimensional grid was generated consisting of the two-dimensional ice shapes and the iced rotor performance was obtained. In this approach a hybrid two/three-dimensional icing analysis was achieved.

Table 1: Summary of Numerical Modelling Approaches for Simulating Rotorcraft Ice Accretion

Authors *(Organisation)*	**Period**	**Approach**	**Flow Analysis**	**Droplet Analysis**	**Icing Analysis**
Britton, Bond, & Flemming [5, 6, 8, 7] *(NASA, Sikorsky Aircaft)*	1991 – 1994	Full 2D	2D	2D	2D
Sankar, Flemming, Kreeger, Bain, Rajmohan, & Nucci [13, 14, 15, 16] *(Georgia Tech, NASA, Sikorsky Aircaft)*	2009 – 2011	Hybrid 2D/3D	3D	2D	2D
Narducci & Kreeger [18, 19] *(The Boeing Company, NASA)*	2010 – 2011	Hybrid 2D/3D	3D	2D	2D
Kelly, Habashi, Quaranta, Masarati, & Fossati [20, 21] *(McGill Uni., Polimi, Uni. Strathclyde)*	2014 – 2018	Hybrid 2D/3D	2D	2D	3D
Chen, Zhao, & Barakos [22, 23, 24] *(Nanjing Uni. of Aeronautics & Astronautics, Uni. of Glasgow)*	2016 – 2019	Full 3D	3D	3D	3D

Between 2010 and 2011 a similar hybrid two/three-dimensional icing approach was published by Narducci and Kreeger [18, 19]. The icing analysis approach developed first established rotor trim, clean rotor performances, and the initial flow-field using a full Navier-Stoked CFD solver coupled with a CSD code. Two-dimensional conditions were extracted at various radial locations along the blade. LEWICE3D [17] was then used to predict a series of two-dimensional ice shapes. A three-dimensional iced rotor was then constructed and the rotor trim and performance was established. Their work highlighted the challenge of directly extracting two-dimensional conditions from a three-dimensional solution. It was assumed that the ice shape is not a strong function of the azimuthal velocity variation and angle-of-attack and can be characterized by a slow-moving blade. The blade motion was then considered as a series of quasi-static events and only the mean and extreme azimuthal velocity variation and angle-of-attack were used.

Between 2014 and 2018, Kelly et al. devised a numerical approach for assessing the degraded aerodynamics and flight characteristics of iced rotors [20, 21]. A trimmed flight condition was initially found through the use of a multibody approach for rotor dynamics to determine the angle-of-attack and incident velocity. The aero-icing module FENSAP-ICE [25] simulated the ice accretion and determined performance degradation. To simulate the ice accretion, a hybrid two/three-dimensional approach was developed in which the blade was discretized into two-dimensional sections along the blade span and the aerodynamics and droplet impingement are computed. Three-dimensional fields of the aerodynamic quantities and droplet dynamics were then interpolated over the blade surface to enable three-dimensional ice accretion. The blade surface mesh was then rotated during the icing process allowing for spanwise motion of the liquid film generated by centrifugal forces.

Hybrid two/three-dimensional approaches have provided an encouraging insight into the potential of numerical techniques for rotorcraft icing. However, reservations should be had of results using this approach given that rotorcraft are primarily dominated by three-dimensional flow features and any two-

dimensional assumption is limiting. Fully three-dimensional rotorcraft icing codes are therefore taking precedence over hybrid approaches, with numerical limitations being the major constraint in technological advancements.

Between 2016 and 2019 the first attempt to model rotor icing using a fully three-dimensional approach was made by Chen and Zhao from Nanjing University of Aeronautics and Astronautics [22, 23, 24] and Barakos from the University of Glasgow. A new method for predicting three-dimensional ice accretion on rotors was proposed. The CLORNS code was used to determine the aerodynamic characteristics of an unsteady iced rotor flow-field [26]. A three-dimensional Eulerian method with a shadow zone dispersion model was developed for computing the droplet trajectories and collection efficiency [27]. An icing model based on the classical Messinger model [11] and a new model to account for the movement of the liquid film in the centrifugal direction [23] was used. In this approach, there were no two-dimensional assumptions introduced. The numerical method was demonstrated on a rotor blade in hover and forward flight.

However, even this latest three-dimensional approach is not without its own limitations. Eulerian particle tracking approaches are appealing for three-dimensional problems due to their high efficiency, however, they potentially fail to account for the fundamental physics of the individual supercooled water droplets. Behaviour which is difficult to capture using an Eulerian approach includes the trajectories of secondary particles during splashing on impact and particle breakup. The splashing of particles has been demonstrated as of first-order importance while simulating supercooled large water droplets [28, 29]. Moreover, icing models based on the classical Messinger model have been shown to under-predict the rate of ice accretion [30].

The remainder of this work seeks to provide a new high-fidelity approach for the modelling of rotorcraft icing using entirely three-dimensional techniques to address the weaknesses highlighted within the literature. This new approach will be demonstrated throughout the remainder of this work on a model rotor in forward flight. The operation of the SRB-II model rotor, when exposed to

a range of icing conditions, has been identified for validation of the numerical predictions. The experimental measurements will allow for metrics such as the ice thickness and shape to be compared at various radial locations. Intriguingly, ice shedding measurements were also recorded allowing for the assessment of ice shedding prediction capabilities. In the past, numerical ice shedding analyses have been based on a series of two-dimensional ice accretion computations to determine the mass and radial location of shed ice [31, 32]. Given that ice shedding is quintessentially three-dimensional, this is a significant limitation. To address this limitation, this work seeks to introduce an entirely three-dimensional numerical ice shedding approach.

The organisation of this work follows the subsequent structure; the SRB-II model is introduced in detail in Section 4, the collective suite of numerical tool used for ice prediction are discussed in Section 2, the numerical ice prediction results are presented in Section 5, finally the concluding remarks from this work are outlined in Section 6.

2. Ice Prediction Framework

2.1. Aerodynamic Analysis

The SU2 software suite [33] is an open-source toolkit written in C++ and Python created for multi-physics simulation and design. The core of the suite is a Reynolds-averaged Navier-Stokes (RANS) solver which is used in this study in tandem with the Spalart–Allmaras (SA) turbulence model. These mass, momentum, and energy conservation equations can be summarised as,

$$\frac{\partial U}{\partial t} + \nabla \cdot \boldsymbol{F}^{c}_{ale} - \nabla \cdot (\mu^{1}_{tot}\boldsymbol{F}^{v1} + \mu^{2}_{tot}\boldsymbol{F}^{v2}) = \boldsymbol{Q} \quad \text{in} \quad \Omega, \quad t > 0 \tag{1}$$

where the vector of conservative variables is represented by, $\boldsymbol{U} = \{\rho,\, \rho\boldsymbol{v},\, \rho E\}^{T}$, in the flow domain, Ω. The fluid density, flow velocity vector, static pressure, temperature and total energy per unit mass are respectively given by the orthodox notation ρ, $\boldsymbol{v}$, p, T, E.

Finite volume method (FVM) is applied on arbitrary unstructured meshes using a standard edge-based data structure on a dual grid with control volumes constructed using a median-dual, vertex-based scheme. Regarding time integration, SU2 is capable to solve implicitly steady and unsteady problems, using a dual-time stepping strategy, leading to second-order accuracy in space and time. The application towards its use for the simulation of rotorcraft flows has recently been highlighted by Ref.[34].

2.2. Particle Tracking

An in-house particle tracking code based on a Lagrangian framework was developed at Politecnico di Milano and is used for the simulation of clouds containing supercooled water droplets [35]. The Lagrangian framework permits the modelling of supercooled water droplets at an individual particle level. Subsequently, fundamental physics such as particle splashing on impact can be modelled. The following system of ordinary differential equations is used to compute the particle positions:

$$\begin{cases} \dfrac{d\mathbf{u}_p}{dt} = \dfrac{3}{4}\dfrac{\mu_f Re_p C_D}{\rho_p d_p^2}(\mathbf{u}_f - \mathbf{u}_p) + \mathbf{g}\left(1 - \dfrac{\rho_f}{\rho_p}\right) \\ \dfrac{d\mathbf{x}_p}{dt} = \mathbf{u}_p \end{cases} \tag{2}$$

where the subscripts p and f are representative of the particle and fluid. Additionally, μ, ρ, and $\mathbf{u}$ denote the gas viscosity, density and velocity at the particle position, $\mathbf{x}_p$. The gravity vector is given by $\mathbf{g}$. While the diameter of each particle is represented by d. Finally, the particle drag coefficient and Reynolds number can respectively be described by C_D and Re. An assumption is that only the aerodynamic drag, gravity and particle inertia influence the particle trajectory. Although effects including particle-particle interactions and deformable particles may also influence the final trajectory they are currently not considered.

The particle Reynolds number describes the relative flow around the particle. The drag force acting on any given particle is a combination of the models from Morrison [36] and Clift et al. [37] to best fit experimental data and is given by,

$$C_D = \begin{cases} \dfrac{24}{Re_p} + 2.6\dfrac{\frac{Re_p}{5}}{1+\left(\frac{Re_p}{5}\right)^{1.52}} + 0.411\dfrac{\left(\frac{Re_p}{263000}\right)^{-7.94}}{1+\left(\frac{Re_p}{263000}\right)^{-8}} + 0.25\dfrac{\frac{Re_p}{10^6}}{1+\frac{Re_p}{10^6}} & Re_p \leq 10^6 \\ 0.19 - \dfrac{8\cdot 10^4}{Re_p} + \delta & Re_p > 10^6 \end{cases} \tag{3}$$

Techniques to allow for particle tracking in mesh with arbitrary motion and across non-conformal boundary interfaces are used within this work to simulate clouds entrained within rotorcraft flow-fields [38].

2.3. Ice Accretion

The in-house code PoliMIce is used for computing the ice accretion [39]. The PoliMIce software library provides state-of-the-art ice formation models including the Myers model [30], the modified Myers model [40], and the local exact solution of the Stefan problem [41]. Myers introduced a rime limit thickness, B_g, as a criterion for the selection of the ice regime. The rime ice limit thickness describes the condition at which the glaze regime can first appears. If the ice thickness $B < B_g$ or $B_g < 0$: the *rime* ice accretion law is used, while if the ice thickness $B > B_g$: the *glaze* ice accretion law is used. The rate of rime ice accretion can then be written as,

$$\frac{\partial B}{\partial t} = \frac{\beta LWC V_\infty}{\rho_{\text{rime}}} \tag{4}$$

while the rate of glaze ice accretion reads,

$$\frac{\partial B}{\partial t} = \frac{1}{\rho_{\text{glaze}} L_F}(\dot{Q}_{down} + \dot{Q}_{up}) \tag{5}$$

where the collection efficiency, droplet liquid water content and freestream velocity are respectively denoted by β, LWC, and V_∞. Here ρ represents the density of ice which depends on the ice regime. $\dot{Q}_{down}$ and $\dot{Q}_{up}$ are the heat fluxes exchanged on the ice/water phase change interface. L_F is the latent heat required for melting ice.

The model used in this work to capture the complex experimental ice shapes is the local exact solution of the unsteady Stefan problem for the temperature profiles within the ice layer in glaze conditions [41]. The ice shapes are then computed using a multi-step approach, whereby non-linear ice accretion is accounted for by iteratively updating the surface solution on which the ice accretes. The efficacy of the approach for predicting ice shapes on two-dimensional oscillating airfoils is highlighted in Ref.[42].

2.4. Ice Shedding

In this work, a three-dimensional ice shedding module was introduced into the PoliMIce software for the computation of ice shedding events. The approach radially discretizes the iced rotor into several ice blocks. The summation of the forces acting on each block of ice determines if a shedding event occurs. Shedding is present when the centrifugal forces, $F_{\text{centrifugal}}$, acting on the ice exceeds a combination of both the cohesive force, $F_{\text{conhesive}}$, and adhesive force, F_{adhesive}, of the ice,

$$F_{\text{centrifugal}} > F_{\text{conhesive}} + F_{\text{adhesive}} \tag{6}$$

where the centrifugal, cohesive, and adhesive forces acting on the ice are respectively computed by the following formulae,

$$F_{\text{centrifugal}} = m_{\text{ice}} r\omega, \quad F_{\text{conhesive}} = \sigma A_{\text{ice}}, \quad F_{\text{adhesive}} = \tau A_{\text{surface}} \tag{7}$$

and where the mass of ice is represented by m_{ice}, the cohesion shear stress of ice is represented by σ, the adhesion shear stress of ice is represented by τ. The mass of ice is determined by,

$$m_{\text{ice}} = h\rho_{\text{ice}} A_{\text{surface}} \tag{8}$$

where h is the ice thickness, ρ_{ice} is the density of ice, and A_{surface} is the surface area in contact with the blade substrate. Where the density of ice is dependent on the type of ice, be it rime or glaze.

Ice adhesion models to predict shear stress at shedding were developed by Fortin and Perron [43]. Their work measured the adhesion shear stress between the 6066-T6 aluminium substrate of the SRB-II rotor and the accreted ice. The adhesion shear stress measurements are shown in Fig. 2. An empirical relationship between the adhesion shear stress and temperature on the SRB-II rotor can subsequently be determined,

$$\tau = -0.0132806\,T + 3.62295 \tag{9}$$

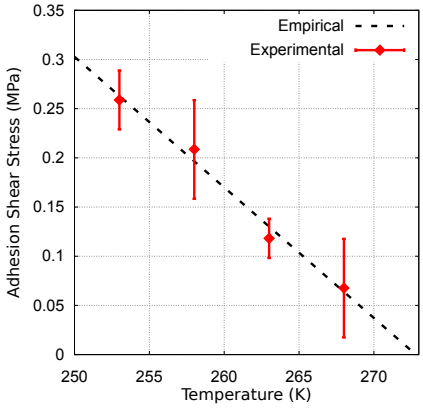

Figure 2: Experimental adhesion shear stress vs temperature results on the SRB-II Aluminium substrate taken from Ref.[43]. Where the empirical relationship of the adhesive shear stress vs temperature is based on $\tau = -0.0132806\,T + 3.62295$.

Additionally, a cohesive ice model was developed by Fortin and Perron as part of the SRB-II experimental rotor icing tests [43, 44]. Their model is summarised. It indicates that under increasing tensile load, crack nucleation begins when the normal stress is approximately 0.5 MPa. Cracks then increase in size and when the strain reaches the critical grain boundary value proportionate to a critical wedge displacement of $x_c = 0.47$ µm, crack propagation takes place. Subsequently, cohesive failure occurs and the ice breaks. While considering that viscoplastic strain is negligible during rotor ice accretion, the cohesive failure

stress can be expressed as,

$$\sigma = \left(\frac{x_c}{9 \times 10^{-3} + d} \right) E\left(T\right) \tag{10}$$

where the Young's modulus of ice and grain size are respectively denoted by $E\left(T\right)$ and d. Each of which are temperature dependent. Subsequently, the cohesive force between the blocks of ice is computed and requires the cross sectional area, A_{ice}, at each block interface. The steps for computing the cross sectional area at each block interface is subsequently described and a schematic of the routine is illustrated in Fig. 3:

1. Compute the normalized radial distance to the centroid of E_A.
2. Identify the shared nodes of E_A to find E_B.
3. Compute the distance between N_1 and N_2.
4. Calculate the ice thickness h, at the intersection.
5. Calculate the cross sectional area A_{ice}, of the block interface.

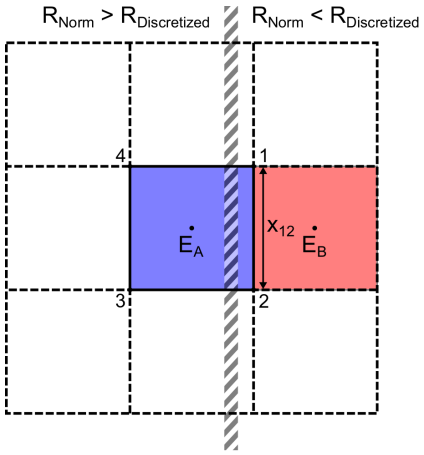

Figure 3: Schematic illustrating the method for computing the cross sectional area at each block interface to determine the cohesive force.

2.5. Mesh Deformation

Radial Basis Function Mesh Deformation (RBF) mesh deformation techniques are used to update the iced mesh. RBF mesh deformation techniques

are robust and preserve high-quality mesh even during large deformations. Furthermore, the potential of RBF mesh deformation techniques for non-smooth, local deformations such as those present during aircraft icing has been demonstrated by Ref.[45].

The term radial basis function refers to a series of functions whose values depends on their distance to a supporting position. In the most general of forms, radial basis functions can be written as, $\phi(\mathbf{r}, \mathbf{r}_i) = \phi\left(\|\mathbf{r} - \mathbf{r}_i\|\right)$, where the distance corresponds to the radial basis centre, $\mathbf{r}_i$. This distance is frequently taken as the Euclidean distance, meaning it becomes the spatial distance between two nodes. An interpolation function, $f(\mathbf{r})$ can be introduced as a method for describing the displacement of a set of nodes in space and can be approximated by a weighted sum of basis functions. The interpolation takes the form

$$f(\mathbf{r}) = \sum_{i=1}^{N} \alpha_i \phi\left(\|\mathbf{r} - \mathbf{r}_i\|\right) \tag{11}$$

However, it is computational prohibitive to use standard RBF mesh deformation on large data sets. To address this concern, multi-level greedy surface point selection algorithms [46] and volume point reduction methods [47] are introduced to improve the computational expense of RBF mesh deformation.

3. Model Validation

The collection of high-quality experimental ice accretion measurements for rotorcraft is challenging, limiting the data available for validation. For this reason, several well-known fixed-wing experimental test cases have been selected for preliminary validation of the three-dimensional ice accretion models. The first experimental text case selected is for the validation of the collection efficiency model on a full-scale horizontal swept tail [48]. The second test case selected is for the validation of the predicted ice shapes on a wing with various sweep angles [49].

3.1. Droplet Impingement

The extensive experimental database from Papadakis et al. [48] is used for the validation of water droplet impingement models. The experimental tests were conducted in the NASA Glenn Icing Research Tunnel (IRT) on a range of configurations and included measurements of the flow and droplet impingement. The configuration selected here is the outboard portion of a full-scale horizontal swept tail from a general business jet with a NACA 64A008 profile. The operating conditions are shown in Table 2 and are representative of Appendix C conditions.

Table 2: Horizontal Tail Test Conditions Ref. [48].

Mach [–]	AoA [°]	Pressure [Pa]	Temp [K]	MVD [g/m^3]	Re [–]	Chord [in]
0.23	6.0	83,025	291.2	21	5.03×10^6	37.65

The flow field prediction is first compared with the experimental measurements in Fig. 4 at two spanwise stations. The location of the two spanwise stations are shown in Fig. 4a. While the numerical predictions of the pressure coefficient distribution are compared to the experimental measurements in Figs. 4b & 4b. In general, the pressure coefficient distribution is in close agreement with the measurements on both the upper and lower surface of the wing and the leading edge suction peak is captured.

The water droplet impingement model is compared with the experimental recordings in Fig. 5. Impingement data was again obtained at two spanwise stations as shown in Fog. 5a. However the experimental data was reduced to the most inboard station due to high similarity in the measurements. The prediction of the collection efficiency on the swept horizontal tail is shown in Fig. 5b. The collection efficiency peak and droplet impingement limits are well represented.

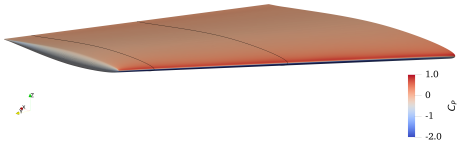

(a) Surface pressure coefficient distribution with selected spanwise stations.

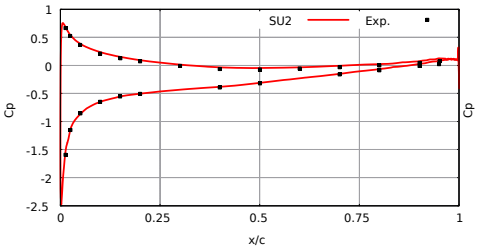

(b) Pressure coefficient distribution at the inboard location $y = 24$ in.

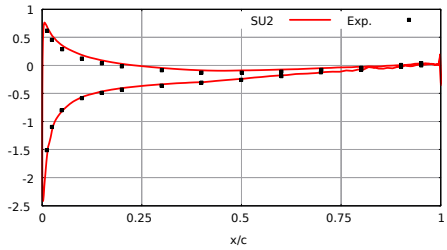

(c) Pressure coefficient distribution at the inboard location $y = 43$ in.

Figure 4: NACA 64A008 swept tail pressure coefficient distribution at two inboard and outboard spanwise locations compared to experimental data from Ref.[48].

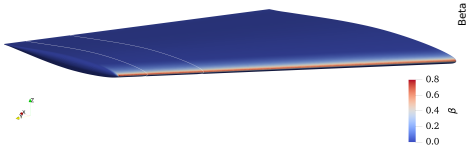

(a) β at the inboard location $y = 36$ in.

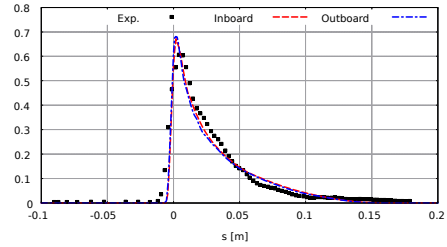

(b) β at the inboard location $y = 44$ in.

Figure 5: NACA 64A008 swept tail collection efficiency, β, with a MVD = 21µm compared to experimental data from Ref.[48] at two inboard and outboard spanwise locations.

3.2. Ice Accretion

The experimental ice tracings measured by Bidwell [49] on a wing with 30° and 45° sweep angles in the NASA IRT are used for validation of the ice prediction models. The model wing has a symmetric NACA 0012 profile and the wing tunnel operating conditions are shown in Table 3. The swept wing geometry is displayed in Fig. 6.

Table 3: NACA 0012 Swept Wing Test Conditions Ref. [49].

Mach [–]	AoA [°]	Temp [K]	Pressure [Pa]	MVD [µm]	LWC [g/m^3]	Re [–]	Chord [in]
0.3	0.0	257, 266	92321, 94463	32	0.45, 0.47	7.2×10^6	36

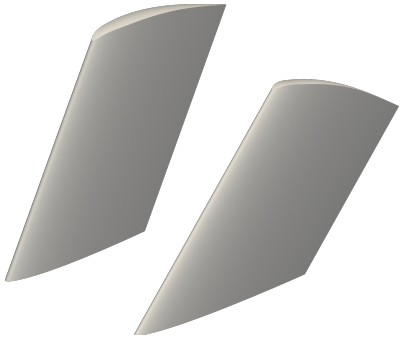

Figure 6: NACA 0012 Swept wing geometry at 30° and 45° sweep angles.

The results of the ice prediction models on the 30° and 45° swept wings at two different operating temperatures are respectively shown in Figs. 7 & 8. The lower temperature operating conditions representative of the rime ice regime are shown in Figs. 7a & 8a. The ice accretion models capture the *spearhead* ice shape characteristic of rime ice regime. The higher temperature operating conditions where the glaze ice regime dominates are shown in Figs. 7b & 8b. Significantly the ice accretion models also capture the more challenging *double-horn* glaze ice structures.

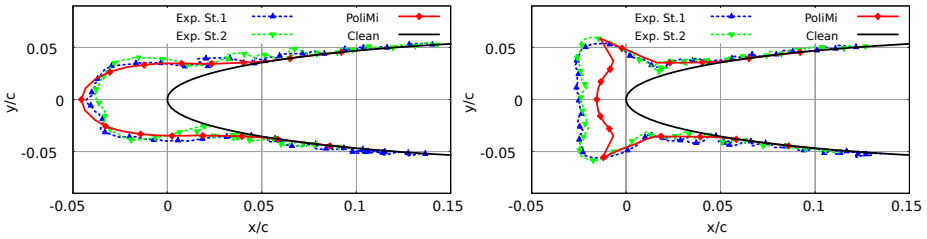

(a) 257K. (b) 266K.

Figure 7: Ice shape comparison with experimental measurements on the 30° swept wing from Ref. [49] during both the rime and glaze ice regime.

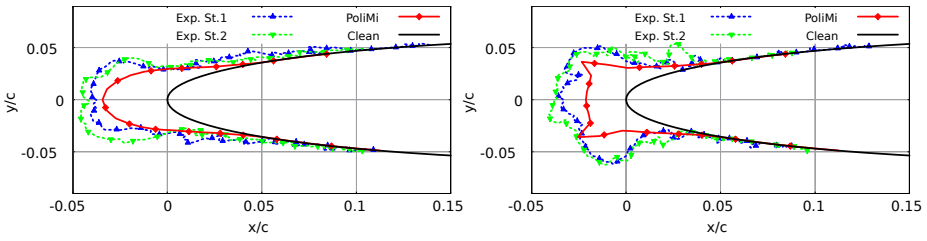

(a) 257K. (b) 266K.

Figure 8: Ice shape comparison with experimental measurements on the 45° swept wing from Ref. [49] during both the rime and glaze ice regime.

4. SRB-II Model

In 2006, the Spinning Rotor Blade (SRB) experimental apparatus was developed at the Anti-icing Material International Laboratory (AMIL) in the Université du Québec à Chicoutimi (UQAC), Canada, in collaboration with Bell Helicopter, Textron [44]. The set up provided a cost-effective and repeatable source of icing wind tunnel data for the development of de-icing systems. Between April, 2006 and June, 2008, the SRB-II configuration performed a standardized test based on typical in-flight icing conditions representative of a continuous icing cloud for helicopters. The influence of the outside air temperature was also critically assessed under these conditions. In total, 155 tests were performed. The primary objective of these tests was to investigate ice physics and the use of hydrophobic coatings for de-icing systems on small helicopters. An extensive number of tests were also used to evaluate the test reproducibility and wind tunnel behaviour.

The AMIL Icing Wind Tunnel (IWT) is a closed-loop, low-speed wind tunnel which operates at subzero temperatures. Throughout the set of standardized tests, the free-stream airspeed, outside air temperature (OAT), liquid water content (LWC), and, mean volume diameter (MVD) of the supercooled water droplets is controlled in the IWT. The hub is connected to a motor to control the rotors rotational speed and the power required to drive the rotor was recorded. The rotor was exposed to the icing cloud until the presence of a shedding event and the length of shed ice was recorded. Finally, the differential between the clean and iced rotor power was recorded. The values of these parameters with their known uncertainty are outlined in Table 4.

The influence of the IWT temperature on the ice structure was assessed. The adhesive shear stress, τ, between the ice and surface substrate was recorded at different temperatures due to its significant impact on the shedding events. Four temperatures were evaluated ranging from a predominantly rime ice regime at $-20°C$, to a predominantly glaze ice regime at $-5°C$. At each temperature, the period of exposure to the icing cloud and iced rotor power was recorded. The

Table 4: SRB-II Standardized Test.

OAT	LWC	MVD	Mach [−]		Shedding	
[K]	[g/m^3]	[µm]	Freestream	Blade-Tip	Time [s]	Length [mm]
258	0.842	26.7	0.046	0.41	130 ± 50	70 ± 15

⋆ Experimental conditions and results taken from Ref. [44].

experimental results are shown in Table 5.

Table 5: SRB-II Temperature Tests.

Tag	OAT	τ	Shedding	
	[K]	[MPa]	Time [s]	Length [mm]
T268	268	0.07 ± 0.02	82 ± 26	123 ± 49
T263	263	0.12 ± 0.03	105 ± 34	111 ± 44
T258	258	0.21 ± 0.06	130 ± 42	70 ± 28
T253	253	0.26 ± 0.08	163 ± 52	36 ± 14

⋆ Experimental conditions and results taken from Ref. [44].

The SRB-II configuration uses a 1/18 sub-scale model helicopter rotor. The blades are constructed from extruded 6066-T6 aluminium. The adhesive shear stress between the ice and the 6066-T6 aluminium substrate decreases with increasing temperature and the relationship is shown in Ref. [43]. The blades are 315 mm in length and are offset from the hub by 75 mm. The blades have a chord of 69.75 mm. The rotor diameter is thus 780 mm. The blades are untwisted and have a NACA0012 profile. Throughout all the standardized and temperature-dependent tests the rotor collective is set at $+6°$, while no cyclic motion was introduced. The rotor geometry and characteristics are summarized by a schematic in Fig. 9.

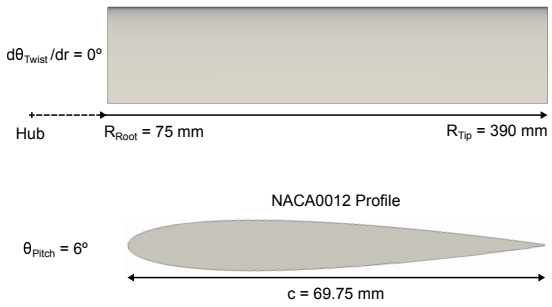

Figure 9: SRB-II model geometry and characteristics.

5. Rotor Ice Prediction Results

Hereinafter, key numerical results obtained during the simulation of the SRB-II model rotor while exposed to icing conditions are presented. The kinetic heating of the blades increases along the blade radius due to the increased rotational velocity of the blade. Subsequently, the ice regime can potentially transition from rime ice near the blade-root to glaze ice near the blade-tip. The ice structures themselves are therefore not only dependent on the outside-air-temperature but also their location radially along the blade. The ice accretion and shedding results for the temperature tests outlined in Table 5 are shown in Fig. 10. The results shown in Fig. 10 allow for a qualitative analysis of the three-dimensional ice structures pre and post-shedding events. In general, it can be observed that the lower temperatures tests exhibit ice structures containing a greater mass of ice prior to shedding events. This is particularly noticeable towards the blade-tip where the ice thickness is greatest. Closer towards the blade-root the quantity of accreted ice is lower and resultantly differences are less clear.

The ice shedding module based on the adhesive shear stress expressed in Eq. 9 allows for the analysis of shedding events in Fig. 10. In particular, it allows for the comparison of the shedding location at various outside-air-temperatures. Although the mass of ice at the lower temperature tests is greater, the value of the adhesion shear stress between the ice and blade surface is higher, and

resultantly, the quantity of ice shed is less. Conversely, at the higher temperature tests, the mass of ice is less, however, since the value of the adhesion shear stress is significantly lower, the quantity of ice shed is greater.

A quantitative analysis of the rotor ice shape numerical predictions based on the environmental conditions from Table 5 is provided in Fig. 11. The results displayed in Fig. 11 help to assess the ice regime at different radial locations during each of the test conditions. Unfortunately, the literature lacks experimental sectional ice shape measurements of the SRB-II model rotor for numerical comparison. During the two test cases at the lowest temperatures namely, $T253$ and $T258$, it can be concluded that rime ice dominates up until around $r/R = 0.8$ due to the ice shapes forming *spearhead* like structures. Radial beyond this, glaze ice dominates due to the ice shapes possessing *double-horn* like structures. During the two highest temperature test cases namely, *T263* and *T268*, it can be concluded that glaze ice dominates at all radial locations. The only portion of ice which appears to remain within the rime ice regime is up until approximately $r/R = 0.6$ during test case *T263*.

An assessment of the ice modelling techniques on the SRB-II model during the standardised test conditions from Table 4 at radial positions $r/R = 0.7$ & 0.9 is provided in Fig. 12. Firstly, a comparison of the standard Myers model [30] with the local, exact solution of the unsteady Stefan problem for temperature profiles within the glaze ice layer as published by Gori et al. [41] is shown in Fig. 12a. The results depict the importance of the local, exact solution of the unsteady Stefan problem for the glaze ice regime towards the blade-tip. The model from Gori et al. [41] is able to capture the ice *horns* whereas, the Myers model [30] is not.

Secondly, the influence of the inclusion of the inertial terms within the liquid film layer is shown in Fig. 12b. The influence of the inertial terms appears significant for this test case under these conditions. As observed in Fig. 11b, rime ice extends to approximately 80% radius. Consequently, the introduction of the inertial terms to the liquid film is only significant beyond this radial location and resultantly, differences are negligible for the rime ice shape at $r/R = 0.7$.

However, at the radial location of $r/R = 0.9$,where glaze ice prevails, the influence of the inertial terms on the liquid film is considerable. Subsequently, the angle of the ice horn is more acute, leading to poorer aerodynamic properties and performance. This finding is contrary to the outcome of the published work from Nanjing University of Aeronautics and Astronautics while using the same test conditions and SRB-II model rotor [23]. Their work suggests negligible differences in glaze ice shapes while comparing the influence of the inertial terms in the liquid film. This highlights the urgent need for advancements in fully three-dimensional rotorcraft icing codes and in particular code-to-code comparison. Furthermore, this is an effect which cannot be captured whilst using hybrid two/three dimensional approaches.

Additionally, it is beneficial to assess the current predictions with the rotor icing code from Nanjing University of Aeronautics and Astronautics [22, 23, 24]. Consequently, a preliminary code-to-code comparison during the standardised test conditions from Table 4 at radial positions $r/R = 0.58$ & 0.84 is provided in Fig. 13. The radial position at $r/R = 0.58$ is shown in Fig. 13a with each code predicting a rime ice shape. The code from Nanjing University of Aeronautics and Astronautics predicts greater asymmetry in the ice shape. The radial position at $r/R = 0.84$ is shown in Fig. 13b with each code predicting significantly different ice shapes. The code from Nanjing University of Aeronautics and Astronautics predicts a similar shape to Fig. 13a however with increased ice thickness. Conversely, the predictions from this work indicate that at this radial position the ice accretion is predominately glaze as depicted by the *horn*-like ice structures. In general, both codes predict ice shapes with a tip thickness within the variations present during the experimental measurements in Ref. [44].

Useful experimental data recorded during the SRB-II icing tests includes information regarding the ice thickness at the blade-tip leading edge. Furthermore, the ice shed location was also recorded. Both sets of data help to partially provide a means of numerical validation. An assessment of the numerical ice thickness predictions at the blade-tip leading edge prior to shedding is shown in Figs. 14a & 14b. The radial variation of the ice thickness at the different

temperatures is shown in Fig. 14a. Overall, there is a slight under prediction of the ice thickness at the blade-tip. However, the non-linearity of the radial ice accretion is importantly highlighted. The experimental variation in ice thickness is displayed in Fig. 14b. The numerical predictions are well within the experimental uncertainties and also align with the empirical relationship outlined in Ref. [44]. The ice shed location at different temperatures is displayed in Fig. 14c. The ice shed location is expressed in terms of the radial position. The adhesion shear stress model is based on a linear relationship with the temperature. Consequently, this is reflected in the numerical prediction of the shed location. The numerical shedding predictions are within the large uncertainty errors recorded during the experimental tests. However, there is quite a significant difference when comparing with the empirical relationship from Ref. [44].

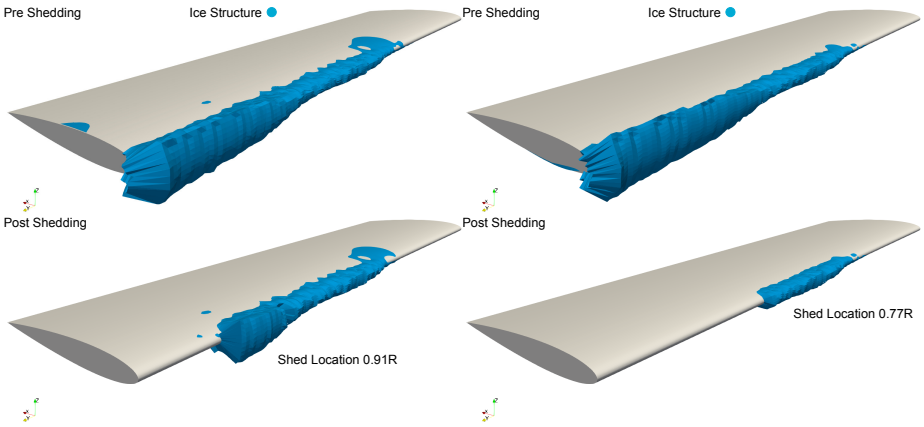

(a) T253.

(b) T258.

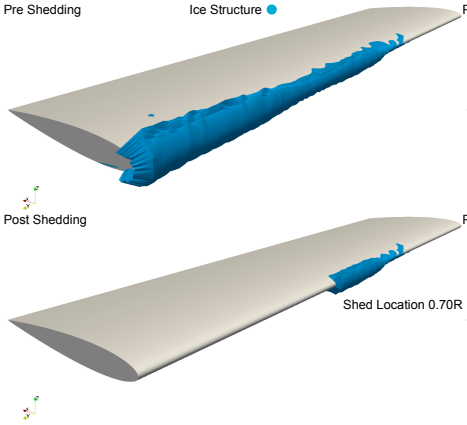

(c) T263.

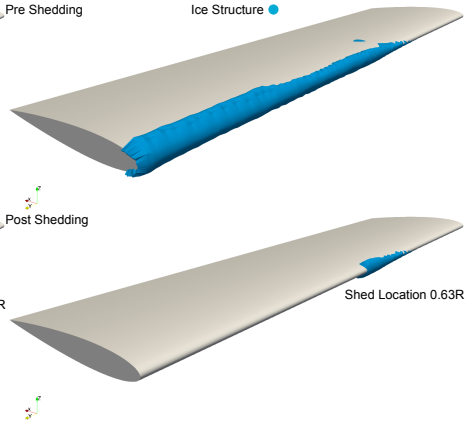

(d) T268.

Figure 10: SRB-II numerical ice shape predictions displayed throughout the temperature dependent conditions outlined in Table 5. Where the ice accretion is represented in blue. Displaying both the instance prior to and post ice shedding events. For each test case, the ice shed location is shown in terms of the radial position.

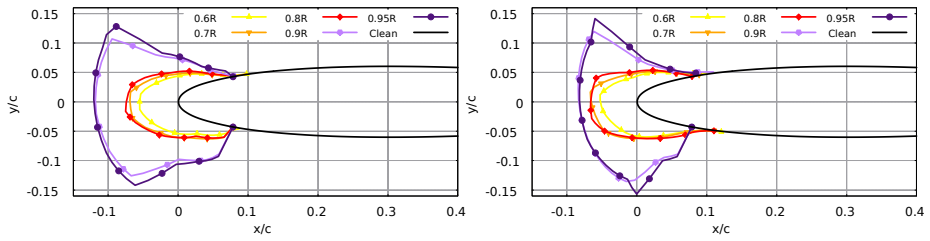

(a) T253.

(b) T258.

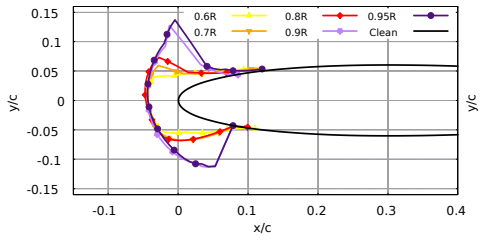

(c) T263.

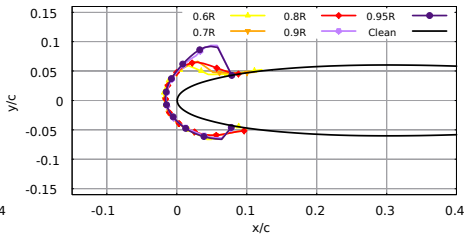

(d) T268.

Figure 11: SRB-II numerical ice shape predictions displayed at selected radial sections for the test conditions outlined in Table 5. Displayed at radial locations r/R = 0.6, 0.7, 0.8, 0.9 & 0.95. The ice shapes are normalized by the rotor chord length and are shown in the $x - y$ plane.

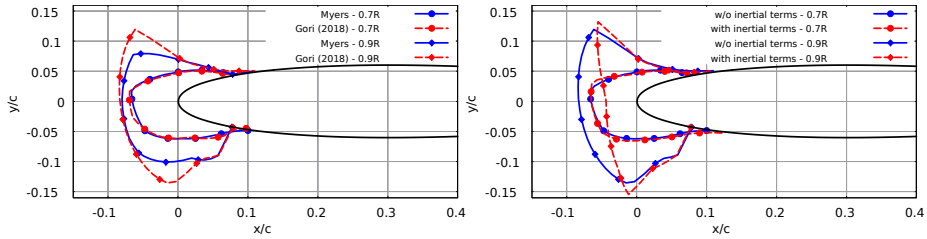

(a) Comparison of icing models. (b) Inclusion of the interial terms in the liquid.

Figure 12: Assessment of ice modelling techniques on the SRB-II model during the standardized test conditions from Table 4 at radial positions $r/R = 0.7\,\&\,0.9$. Firstly, comparing the standard Myers model [30] with the local, exact solution of the unsteady Stefan problem for temperature profiles within the glaze ice layer as published by Gori et al. [41]. Secondly, comparing the influence of the inclusion of the inertial terms within the liquid film layer.

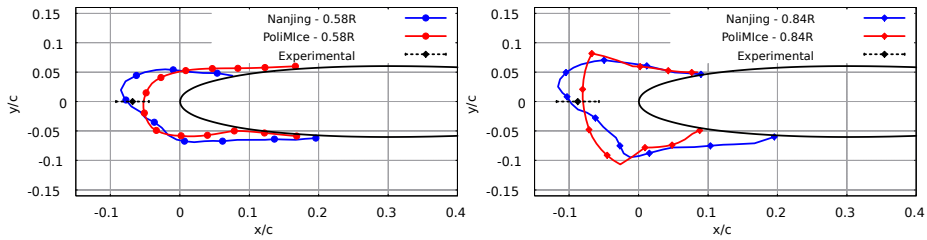

(a) Comparison of codes at $r/R = 58\%$. (b) Comparison of codes at $r/R = 84\%$.

Figure 13: Comparison of numerical predictions with the rotor icing code from authors the at Nanjing University of Aeronautics and Astronautics [22, 23, 24]. Experimental ice thickness measurements taken from Ref. [44]. The selected radial locations were based on the available data.

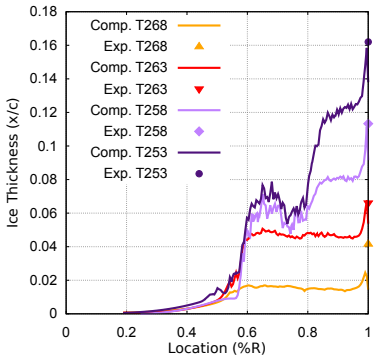

(a) Radial ice thickness.

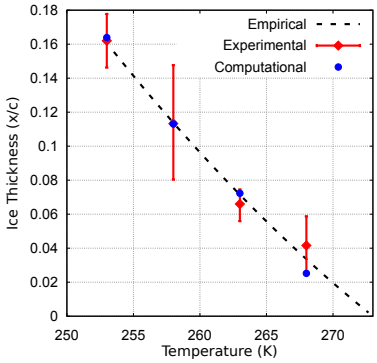

(b) Ice thickness at $r/R = 1$.

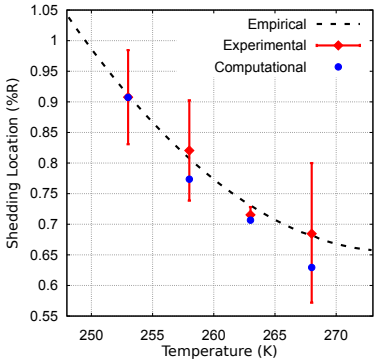

(c) Ice shedding location at $r/R = 1$.

Figure 14: Direct comparison of the computational ice predictions with the experimental and empirical results from Ref. [44] as outlined in Table 5. Firstly, displaying the ice thickness at the leading edge as a function of the radial position. Secondly, showing the ice thickness at the blade-tip with the experimental uncertainties. Thirdly, presenting the ice shedding predictions at the blade-tip.

6. Conclusion

In this work, a novel three-dimensional simulation framework for the prediction of rotorcraft icing is presented. The simulation framework is discussed at an individual solver level and the inter-dependency between the solvers is highlighted. A preliminary validation of the numerical models used in the icing framework is achieved by comparing with high-quality experimental measurements obtained in the NASA IRT. The numerical models used for the prediction of the collection efficiency and ice shapes are shown to be in very good agreement. To that end, even the more challenging glaze ice shapes are well captured. The SRB-II test campaign from the Anti-icing Material International Laboratory in the Université du Québec à Chicoutimi, Canada is then introduced and used as a test case for the simulation of rotorcraft icing. Experimental measurements obtained during the icing tests are compared to the numerical predictions from this work, which include properties such as the ice thickness at the blade-tip and the ice shedding location. Overall, the numerical predictions are in good agreement with the experimental data. Significantly, the numerical predictions underline the non-linearity of the ice accretion radially. Suggesting greater quantities of ice accrete towards the blade-tip, leading to the presence of ice *horns* which are particularly detrimental to rotor performance. Subtleties in the modelling techniques, which subsequently have a significant impact on the final ice shapes, are highlighted. These include the influence of the model for the temperature profile within the ice layer, and appropriate modelling of the liquid film on the blade surface.

Additionally, it is acknowledged that there remain significant limitations to the current simulation framework for simulating rotorcraft icing. The computational cost of the overall icing simulation procedure is very high due to it being unsteady. This means that it is currently not feasible to simulate the entire icing envelope and only selected test points are be considered. Furthermore there are also model simplifications such as the rotor being considered as rigid. There is also key physics which is not included such as the trajectories of the shed

ice. As a result, these limitations and assumptions will look to be addressed in future work.

Acknowledgments

The NITROS (Network for Innovative Training on ROtorcraft Safety) project has received funding from the European Union's Horizon 2020 research and innovation program under the Marie Skłodowska-Curie grant agreement No. 721920.

References

[1] R. Gent, N. Dart, J. Cansdale, Aircraft Icing, Philosophical Transactions of the Royal Society of London. Series A: Mathematical, Physical and Engineering Sciences 358 (1776) (2000) 2873–2911, https://doi.org/10.1098/rsta.2000.0689.

[2] Y. Cao, W. Tan, Z. Wu, Aircraft icing: An ongoing threat to aviation safety, Aerospace Science and Technology 75 (2018) 353–385.

[3] Y. Cao, C. Ma, Q. Zhang, J. Sheridan, Numerical simulation of ice accretions on an aircraft wing, Aerospace Science and Technology 23 (1) (2012) 296–304.

[4] M. Costes, F. Moens, Advanced numerical prediction of iced airfoil aerodynamics, Aerospace Science and Technology 91 (2019) 186–207.

[5] R. Britton, T. Bond, A Review of Ice Accretion Data From a Model Rotor Icing Test and Comparison With Theory, in: 29th Aerospace Sciences Meeting, Reno, Nevada, USA, January 1991, p. 661.

[6] R. Britton, Development of an Analytical Method to Predict Helicopter Main Rotor Performance in Icing Conditions, in: 30th Aerospace Sciences Meeting and Exhibit, Reno, Nevada, USA, January 1992, p. 418.

[7] R. J. Flemming, R. K. Britton, T. H. Bond, Role of Wind Tunnels and Computer Codes in the Certification and Qualification of Rotorcraft for Flight in Forecast Icing, in: 20th European Rotorcraft Forum, Amsterdam, Netherlands, October 1994.

[8] R. Britton, T. Bond, R. Flemming, An Overview of a Model Rotor Icing Test in the NASA Lewis Icing Research Tunnel, in: 32nd Aerospace Sciences Meeting and Exhibit, Reno, Nevada, USA, January 1994, p. 716.

[9] W. B. Wright, Users manual for the improved NASA Lewis ice accretion code LEWICE 1.6, NASA Contractor Report No.198355, June 1995.

[10] J. L. Hess, A. O. Smith, Calculation of Potential Flow About Arbitrary Bodies, Progress in Aerospace Sciences 8 (1967) 1–138.

[11] B. L. Messinger, Equilibrium Temperature of an Unheated Icing Surface as a Function of Air Speed, Journal of the aeronautical sciences 20 (1) (1953) 29–42.

[12] J, Hall and J, Hammerschmidt and J, Goglia and G, Black, National Transportation Safety Board Aviation Accident Final Report, NTSB/AAR-96/01 (July 1996).

[13] J. Bain, L. Sankar, T. Egolf, R. Flemming, R. Kreeger, Progress Towards Modeling the Effects of Ice Accretion on Rotorcraft Performance in Hover and Forward Flight, in: 35th European Rotorcraft Forum, Hamburg, Germany, September 2009.

[14] N. Rajmohan, J. Bain, M. Nucci, L. Sankar, R. Flemming, T. A. Egolf, R. Kreeger, Icing Studies for the UH-60A Rotor in Forward Flight, in: American Helicopter Socitety Aeromechanics Specialists Conference, San Francisco, California, USA, January 2010.

[15] M. Nucci, J. Bain, L. Sankar, T. A. Egolf, R. Flemming, E. Kreeger, A Methodology for Modeling the Effects of Icing on Rotary Wing Aerodynamics, in: 48th AIAA Aerospace Sciences Meeting, Orlando, Florida, USA, January 2010.

[16] J. Bain, R. Deresz, L. Sankar, T. A. Egolf, R. Flemming, E. Kreeger, Effects of Icing on Rotary Wing Loads and Surface Heat Transfer, in: 49th AIAA Aerospace Sciences Meeting including the New Horizons Forum and Aerospace Exposition, Orlando, Florida, USA, January 2011, p. 1100.

[17] C. S. Bidwell, M. G. Potapczuk, Users manual for the NASA Lewis three-dimensional ice accretion code (LEWICE 3D), NASA Technical Memorandum No. 105974, Cleveland, Ohio, USA, December 1993.

[18] R. Narducci, R. E. Kreeger, Analysis of a Hovering Rotor in Icing Conditions, in: American Helicopter Society 66th Annual Forum, Phoenix, Arizona, USA, 2010.

[19] R. Narducci, S. Orr, R. E. Kreeger, Application of a High-Fidelity Icing Analysis Method to a Model-Scale Rotor in Forward Flight, in: American Helicopter Society 67th Annual Forum, Virginia Beach, Virginia, USA, May 2011.

[20] D. Kelly, H. Fouladi, M. Fossati, W. G. Habashi, R. Alicino, G. Quaranta, P. Masarati, Assessment of Ice Accretion Effects on Rotor Dynamics via Multi-Body and CFD Approaches, in: 70th American Helicopter Society International Annual Forum 2014, American Helicopter Society, 2014, pp. 1840–1851.

[21] D. Kelly, W. G. Habashi, G. Quaranta, P. Masarati, M. Fossati, Ice Accretion Effects on Helicopter Rotor Performance, via Multibody and CFD Approaches, Journal of Aircraft 55 (3) (2018) 1165–1176.

[22] G.-q. Zhao, Q.-j. Zhao, X. Chen, New 3-D Ice Accretion Method of Hovering Rotor Including Effects of Centrifugal Force, Aerospace Science and Technology 48 (2016) 122–130.

[23] C. Xi, Z. Qi-Jun, Numerical Simulations for Ice Accretion on Rotors Using New Three-Dimensional Icing Model, Journal of Aircraft 54 (4) (2017) 1428–1442.

[24] X. Chen, Q. Zhao, G. Barakos, Numerical Analysis of Aerodynamic Characteristics of Iced Rotor in Forward Flight, AIAA Journal 57 (4) (2019) 1523–1537.

[25] F. Morency, H. Beaugendre, G. Baruzzi, W. Habashi, FENSAP-ICE-A Comprehensive 3D Simulation System for In-Flight Icing, in: 15th AIAA Computational Fluid Dynamics Conference, Anaheim, California, USA, June 2001, p. 2566.

[26] Z. Qijun, Z. Guoqing, W. Bo, W. Qing, S. Yongjie, X. Guohua, Robust Navier-Stokes Method for Predicting Unsteady Flowfield and Aerodynamic Characteristics of Helicopter Rotor, Chinese Journal of Aeronautics 31 (2) (2018) 214–224.

[27] X. Chen, Q.-J. Zhao, Computational Investigations of Water Collection Efficiency on Blades in Unsteady Vortex Flowfield of Rotor, Aerospace Science and Technology 79 (2018) 482–491.

[28] W. Wright, M. Potapczuk, Semi-Empirical Modelling of SLD Physics, in: 42nd AIAA aerospace sciences meeting and exhibit, Reno, Nevada, USA, January 2004, p. 412.

[29] L. Prince Raj, J. Lee, R. Myong, Ice accretion and aerodynamic effects on a multi-element airfoil under SLD icing conditions, Aerospace Science and Technology 85 (2019) 320–333.

[30] T. G. Myers, Extension to the Messinger Model for Aircraft Icing, AIAA journal 39 (2) (2001) 211–218.

[31] A. Gupta, E. Halloran, L. N. Sankar, J. Palacios, R. E. Kreeger, Development and validation of physics based models for ice shedding, in: Proceedings of the 44th European Rotorcraft Forum, Delft, The Netherlands, 19-20 September, 2018.

[32] J. Anthony, W. G. Habashi, Helicopter rotor ice shedding and trajectory analyses in forward flight, Journal of Aircraft (2021) 1–17Https://doi.org/10.2514/1.C036043.

[33] Economon, T. D., and Palacios, F., and Copeland, S. R., and Lukaczyk, T. W., and Alonso, J. J., SU2: An Open-Source Suite for Multiphysics Simulation and Design, AIAA Journal 54 (3) (2015) 828–846, dOI: https://doi.org/10.2514/1.J053813.

[34] M. Morelli, T. Bellosta, A. Guardone, Development and preliminary assessment of the open-source cfd toolkit su2 for rotorcraft flows, Journal of Computational and Applied Mathematics 389 (2021) 113340.

[35] T. Bellosta, G. Parma, A. Guardone, A Robust 3D Particle Tracking Solver for In-Fight Ice Accretion Using Arbitrary Precision Arithmetic, in: VIII International Conference on Computational Methods for Coupled Problems in Science and Engineering, 2019.

[36] F. A. Morrison, An introduction to fluid mechanics, Cambridge University Press, May, 2013, iSBN: 9781107003538.

[37] R. Clift, J. R. Grace, M. E. Weber, Bubbles, drops, and particles, Courier Corporation, January, 2005, iSBN: 0486317749.

[38] M. Morelli, T. Bellosta, A. Guardone, Lagrangian particle tracking in sliding mesh applicable for rotorcraft icing applications, in: 45th European Rotorcraft Forum, Warsaw, Poland, 7-20 September, 2019, pp. 1–13.

[39] Gori, G., and Zocca, M., and Garabelli, M., and Guardone, A., and Quaranta, G., PoliMIce: A Simulation Framework for Three-Dimensional Ice Accretion, Applied Mathematics and Computation 267 (2015) 96–107, dOI: 10.1016/j.amc.2015.05.081.

[40] G. Gori, M. Zocca, A. Guardone, A model for in-flight ice accretion based on the exact solution of the unsteady stefan problem, in: 7th AIAA Atmospheric and Space Environments Conference, AIAA AVIATION, Dallas, Texas, USA, 18 June, 2015, p. 3019.

[41] Gori, G., and Parma, G., and Zocca, M., and Guardone, A., Local Solution to the Unsteady Stefan Problem for In-Flight Ice Accretion Modeling, Journal of Aircraft 55 (1) (2017) 251–262, dOI: https://doi.org/10.2514/1.C034412.

[42] M. Morelli, B. Y. Zhou, A. Guardone, Acoustic characterization of glaze and rime ice structures on an oscillating airfoil via fully unsteady simulations, Journal of the American Helicopter Society 65 (4) (2020) 1–12.

[43] G. Fortin, J. Perron, Ice Adhesion Models to Predict Shear Stress at Shedding, Journal of adhesion science and technology 26 (4-5) (2012) 523–553, dOI: 10.1163/016942411X574835.

[44] G. Fortin, J. Perron, Spinning Rotor Blade Tests in Icing Wind Tunnel, in: 1st AIAA Atmospheric and Space Environments Conference, Session: ASE-11: Icing Aerodynamics, San Antonio, Texas, 22-25 June, 2009, p. 4260, dOI: 10.2514/6.2009-4260.

[45] M. Morelli, T. Bellosta, A. Guardone, Efficient radial basis function mesh deformation methods for aircraft icing, Journal of Computational and Applied Mathematics 392 (2021) 113492.

[46] G. Wang, H. H. Mian, Z.-Y. Ye, J.-D. Lee, Improved Point Selection Method for Hybrid-Unstructured Mesh Deformation Using Radial Basis Functions, AIAA Journal 53 (4) (2015) 1016–1025, https://doi.org/10.2514/1.J053304.

[47] L. Xie, H. Liu, Efficient Mesh Motion Using Radial Basis Functions With Volume Grid Points Reduction Algorithm, Journal of Computational Physics 348 (2017) 401–415, https://doi.org/10.1016/j.jcp.2017.07.042.

[48] M. Papadakis, K. E. Hung, G. T. Vu, H. W. Yeong, C. S. Bidwell, M. D. Breer, T. J. Bencic, Experimental Investigation of Water Droplet Impingement on Airfoils, Finite Wings, and an S-Duct Engine Inlet, National Aeronautics and Space Administration, Glenn Research Center, Technical Memorandum No. 2002-211700, October 2002.

[49] C. S. Bidwell, Icing Analysis of a Swept NACA 0012 Wing Using LEWICE3D Version 3.48, in: 6th AIAA Atmospheric and Space Environments Conference, Atlanta, GA, USA, 16-20 June, 2014,

https://doi.org/10.2514/6.2014-2200. arXiv:https://arc.aiaa.org/doi/pdf/10.2514/6.2014-2200.
URL https://arc.aiaa.org/doi/abs/10.2514/6.2014-2200